

## Supporting Information:

---

# Quantifying methyl tunneling induced (de)coherence of nitroxides in glassy ortho-terphenyl at low temperatures

Andrea Eggeling,<sup>a</sup> Janne Soetbeer,<sup>a</sup> Luis Fábregas Ibáñez,<sup>a</sup> Daniel Klose,<sup>a</sup> Gunnar Jeschke<sup>\*a</sup>

<sup>a</sup>ETH Zurich, Laboratory of Physical Chemistry, Vladimir-Prelog-Weg 2, 8093 Zurich, Switzerland

---

## Contents

<b>S1 Full state Hamiltonian in uncoupled and coupled rotor basis</b>	<b>2</b>
<b>S2 Tunneling ESEEM contributions in non-parametric rotation barrier distributions</b>	<b>3</b>
<b>S3 Influence of moving mean filter on deuterium nuclear ESEEM</b>	<b>5</b>
<b>S4 Temperature-dependent Hahn echo decay fits with a Gaussian distribution model</b>	<b>5</b>
H-mNOHex in protonated matrix (OTP) - individual fits . . . . .	6
H-mNOHex in deuterated matrix (dOTP) - individual fits . . . . .	7
H-mNOHex in protonated (OTP) and deuterated matrix (dOTP) - global fits . . . . .	8
Comparison of individual and global rotation barrier distributions . . . . .	10
<b>S5 Influence of orientation averaging on tunneling ESEEM contribution</b>	<b>10</b>
<b>S6 Temperature-dependent comparison of SE, SSE and MQR model</b>	<b>11</b>
<b>S7 Temperature dependence of low frequency oscillation in SE fit residual</b>	<b>11</b>

## S1 Full state Hamiltonian in uncoupled and coupled rotor basis

Generally, the full state Hamiltonian for  $M$  methyl groups coupled to an electron spin can be separated into a spin Hamiltonian and the tunneling Hamiltonian. Considering a single methyl rotor ( $M = 1$ ) coupled to an electron spin, we describe the spin Hamiltonian for all localized methyl group configurations according to Eq. 1 in the paper.

$$\hat{H}(\phi_1 = 0^\circ) = \hat{H}_Z + A_1 \hat{S}_z \hat{S}_{1,z} + A_2 \hat{S}_z \hat{S}_{2,z} + A_3 \hat{S}_z \hat{S}_{3,z} \quad (1)$$

$$\hat{H}(\phi_2 = 120^\circ) = \hat{H}_Z + A_2 \hat{S}_z \hat{S}_{1,z} + A_3 \hat{S}_z \hat{S}_{2,z} + A_1 \hat{S}_z \hat{S}_{3,z} \quad (2)$$

$$\hat{H}(\phi_3 = 240^\circ) = \hat{H}_Z + A_3 \hat{S}_z \hat{S}_{1,z} + A_1 \hat{S}_z \hat{S}_{2,z} + A_2 \hat{S}_z \hat{S}_{3,z} . \quad (3)$$

The spin Hamiltonian for each localized rotor configuration is inserted on the diagonal in the  $3 \times 3$  tunneling Hamiltonian matrix which connects the rotor states by off-diagonal elements corresponding to  $-\frac{V_i}{3}$ . When two methyl groups  $M = 2$  are coupled to the same electron spin simultaneously, they can either be considered as individual rotors or as coupled rotors. If they are treated as single rotors that do not interact with each other, the spin Hamiltonian for each localized rotor state of methyl group  $m = 2$  takes the form

$$\hat{H}(\psi_1 = 0^\circ) = \hat{H}_Z + A_4 \hat{S}_z \hat{S}_{4,z} + A_5 \hat{S}_z \hat{S}_{5,z} + A_6 \hat{S}_z \hat{S}_{6,z} \quad (4)$$

$$\hat{H}(\psi_2 = 120^\circ) = \hat{H}_Z + A_5 \hat{S}_z \hat{S}_{4,z} + A_6 \hat{S}_z \hat{S}_{5,z} + A_4 \hat{S}_z \hat{S}_{6,z} \quad (5)$$

$$\hat{H}(\psi_3 = 240^\circ) = \hat{H}_Z + A_6 \hat{S}_z \hat{S}_{4,z} + A_4 \hat{S}_z \hat{S}_{5,z} + A_5 \hat{S}_z \hat{S}_{6,z} . \quad (6)$$

The full Hamiltonian for both methyl groups is prepared according to the procedure described above, yielding individual total Hamiltonian matrices for methyl groups  $m$  with mixing terms depending on the rotors tunneling frequency  $\nu_{i,m}$ . A visualization of the individual full state Hamiltonians for  $M = 2$  is presented in Fig. S1a–b.

In case of two coupled methyl groups, a coupled rotor basis is needed to express the tunneling Hamiltonian, which becomes a  $9 \times 9$  matrix. The tunneling Hamiltonian represents all combinations of the three energy states ( $A_1, E_{a,1}, E_{b,1}$ ,  $A_2, E_{a,2}, E_{b,2}$ ) of the librational ground state of both rotors ( $r = 0$ ). Methyl tunneling of the individual rotors is enabled by the off-diagonal mixing terms which connect the localized states of methyl groups  $m = 1$  and  $m = 2$ , respectively. The spin Hamiltonian for all combinations of the localized configurations of both methyl groups according to Eq. 5 in the paper

$$\hat{H}(\phi_1, \psi_1) = \hat{H}_Z + A_1 \hat{S}_z \hat{S}_{1,z} + A_2 \hat{S}_z \hat{S}_{2,z} + A_3 \hat{S}_z \hat{S}_{3,z} + A_4 \hat{S}_z \hat{S}_{4,z} + A_5 \hat{S}_z \hat{S}_{5,z} + A_6 \hat{S}_z \hat{S}_{6,z} \quad (7)$$

$$\hat{H}(\phi_2, \psi_1) = \hat{H}_Z + A_2 \hat{S}_z \hat{S}_{1,z} + A_3 \hat{S}_z \hat{S}_{2,z} + A_1 \hat{S}_z \hat{S}_{3,z} + A_4 \hat{S}_z \hat{S}_{4,z} + A_5 \hat{S}_z \hat{S}_{5,z} + A_6 \hat{S}_z \hat{S}_{6,z} \quad (8)$$

$$\hat{H}(\phi_3, \psi_1) = \hat{H}_Z + A_3 \hat{S}_z \hat{S}_{1,z} + A_1 \hat{S}_z \hat{S}_{2,z} + A_2 \hat{S}_z \hat{S}_{3,z} + A_4 \hat{S}_z \hat{S}_{4,z} + A_5 \hat{S}_z \hat{S}_{5,z} + A_6 \hat{S}_z \hat{S}_{6,z} \quad (9)$$

$$\hat{H}(\phi_1, \psi_2) = \hat{H}_Z + A_1 \hat{S}_z \hat{S}_{1,z} + A_2 \hat{S}_z \hat{S}_{2,z} + A_3 \hat{S}_z \hat{S}_{3,z} + A_5 \hat{S}_z \hat{S}_{4,z} + A_6 \hat{S}_z \hat{S}_{5,z} + A_4 \hat{S}_z \hat{S}_{6,z} \quad (10)$$

$$\hat{H}(\phi_2, \psi_2) = \hat{H}_Z + A_2 \hat{S}_z \hat{S}_{1,z} + A_3 \hat{S}_z \hat{S}_{2,z} + A_1 \hat{S}_z \hat{S}_{3,z} + A_5 \hat{S}_z \hat{S}_{4,z} + A_6 \hat{S}_z \hat{S}_{5,z} + A_4 \hat{S}_z \hat{S}_{6,z} \quad (11)$$

$$\hat{H}(\phi_3, \psi_2) = \hat{H}_Z + A_3 \hat{S}_z \hat{S}_{1,z} + A_1 \hat{S}_z \hat{S}_{2,z} + A_2 \hat{S}_z \hat{S}_{3,z} + A_5 \hat{S}_z \hat{S}_{4,z} + A_6 \hat{S}_z \hat{S}_{5,z} + A_4 \hat{S}_z \hat{S}_{6,z} \quad (12)$$

$$\hat{H}(\phi_1, \psi_3) = \hat{H}_Z + A_1 \hat{S}_z \hat{S}_{1,z} + A_2 \hat{S}_z \hat{S}_{2,z} + A_3 \hat{S}_z \hat{S}_{3,z} + A_6 \hat{S}_z \hat{S}_{4,z} + A_4 \hat{S}_z \hat{S}_{5,z} + A_5 \hat{S}_z \hat{S}_{6,z} \quad (13)$$

$$\hat{H}(\phi_2, \psi_3) = \hat{H}_Z + A_2 \hat{S}_z \hat{S}_{1,z} + A_3 \hat{S}_z \hat{S}_{2,z} + A_1 \hat{S}_z \hat{S}_{3,z} + A_6 \hat{S}_z \hat{S}_{4,z} + A_4 \hat{S}_z \hat{S}_{5,z} + A_5 \hat{S}_z \hat{S}_{6,z} \quad (14)$$

$$\hat{H}(\phi_3, \psi_3) = \hat{H}_Z + A_3 \hat{S}_z \hat{S}_{1,z} + A_1 \hat{S}_z \hat{S}_{2,z} + A_2 \hat{S}_z \hat{S}_{3,z} + A_6 \hat{S}_z \hat{S}_{4,z} + A_4 \hat{S}_z \hat{S}_{5,z} + A_5 \hat{S}_z \hat{S}_{6,z} \quad (15)$$

The localized spin Hamiltonian  $\hat{H}(\phi, \psi)$  is placed on the diagonal of the tunneling Hamiltonian matrix in the coupled basis such that the off-diagonal elements enable tunneling between the rotor configurations ( $\phi_i, \psi_j$ ) of the individual rotors. The full state Hamiltonian in the coupled rotor basis is illustrated in Fig. S1c. If there is rotational coupling between the two methyl groups, several additional off-diagonal terms must be considered as explained by Khazaei et al.<sup>1</sup>. In this work, we set the rotational coupling terms to zero since this interaction is negligible with respect to the tunneling ESEEM of the nitroxide H-mNOHex (see main paper for explanation).

$\hat{H}(\phi_1)$	$-\frac{v_{t,1}}{3}$	$-\frac{v_{t,1}}{3}$
$-\frac{v_{t,1}}{3}$	$\hat{H}(\phi_2)$	$-\frac{v_{t,1}}{3}$
$-\frac{v_{t,1}}{3}$	$-\frac{v_{t,1}}{3}$	$\hat{H}(\phi_3)$

$\hat{H}(\psi_1)$	$-\frac{v_{t,2}}{3}$	$-\frac{v_{t,2}}{3}$
$-\frac{v_{t,2}}{3}$	$\hat{H}(\psi_2)$	$-\frac{v_{t,2}}{3}$
$-\frac{v_{t,2}}{3}$	$-\frac{v_{t,2}}{3}$	$\hat{H}(\psi_3)$

$\hat{H}(\phi_1, \psi_1)$	$-\frac{v_{t,1}}{3}$	$-\frac{v_{t,1}}{3}$	$-\frac{v_{t,2}}{3}$			$-\frac{v_{t,2}}{3}$		
$-\frac{v_{t,1}}{3}$	$\hat{H}(\phi_2, \psi_1)$	$-\frac{v_{t,1}}{3}$		$-\frac{v_{t,2}}{3}$			$-\frac{v_{t,2}}{3}$	
$-\frac{v_{t,1}}{3}$	$-\frac{v_{t,1}}{3}$	$\hat{H}(\phi_3, \psi_1)$				$-\frac{v_{t,2}}{3}$		$-\frac{v_{t,2}}{3}$
$-\frac{v_{t,2}}{3}$			$\hat{H}(\phi_1, \psi_2)$	$-\frac{v_{t,1}}{3}$	$-\frac{v_{t,1}}{3}$	$-\frac{v_{t,2}}{3}$		
	$-\frac{v_{t,2}}{3}$		$-\frac{v_{t,1}}{3}$	$\hat{H}(\phi_2, \psi_2)$	$-\frac{v_{t,1}}{3}$		$-\frac{v_{t,2}}{3}$	
		$-\frac{v_{t,2}}{3}$	$-\frac{v_{t,1}}{3}$	$-\frac{v_{t,1}}{3}$	$\hat{H}(\phi_3, \psi_2)$			$-\frac{v_{t,2}}{3}$
$-\frac{v_{t,2}}{3}$			$-\frac{v_{t,2}}{3}$			$\hat{H}(\phi_1, \psi_3)$	$-\frac{v_{t,1}}{3}$	$-\frac{v_{t,1}}{3}$
	$-\frac{v_{t,2}}{3}$			$-\frac{v_{t,2}}{3}$		$-\frac{v_{t,1}}{3}$	$\hat{H}(\phi_2, \psi_3)$	$-\frac{v_{t,1}}{3}$
		$-\frac{v_{t,2}}{3}$			$-\frac{v_{t,2}}{3}$	$-\frac{v_{t,1}}{3}$	$-\frac{v_{t,1}}{3}$	$\hat{H}(\phi_3, \psi_3)$

Fig. S1 Full state Hamiltonian for two methyl groups coupled to an electron spin considering the tunneling Hamiltonian in their individual uncoupled rotor basis or in a coupled rotor basis. (a) Hamiltonian for an individual uncoupled methyl rotor  $m = 1$  with tunneling frequency  $v_{t,1}$  corresponding to the rotation barrier  $V_{3,1}$  (light blue). (b) Hamiltonian for an individual uncoupled methyl rotor  $m = 2$  with tunneling frequency  $v_{t,2}$  corresponding to the rotation barrier  $V_{3,2}$  (dark blue). (c) Coupled basis Hamiltonian of two uncoupled methyl groups  $m = 1, 2$  with their respective tunneling frequencies  $v_{t,1}$  and  $v_{t,2}$ . The rotational coupling terms are omitted since rotational coupling is negligible for the investigated spin system.

## S2 Tunneling ESEEM contributions in non-parametric rotation barrier distributions

The different contributions of the extracted non-parametric rotation barrier distributions for H-mNOHex in OTP and dOTP at Q- and W-band were analyzed individually by evaluating their corresponding tunneling ESEEM signal. The rotation barrier distribution was split into three regions separating all significant contributions. The related tunneling ESEEM signal was calculated by

$$V_{2\text{ptE}}(2\tau) \Big|_{V_{3,\text{start}}}^{V_{3,\text{stop}}} = \int_{V_{3,\text{start}}}^{V_{3,\text{stop}}} dV_3 K(2\tau, V_3) P(V_3) \quad (16)$$

where the integration window for the analyzed distribution region is limited by  $V_{3,\text{start}}$  and  $V_{3,\text{stop}}$ . The scaling was adjusted to match the scale of the overall tunneling ESEEM signal.

The results for H-mNOHex in OTP at 40 K at Q-band and W-band frequencies are presented in Fig. S2a–b. The different tunneling ESEEM contributions for H-mNOHex measured at 10 K in OTP are shown Fig. S2c and for dOTP in Fig. S2d. Generally, the distribution mass at low rotation barriers, which correspond to high tunneling frequencies, fits the nuclear ESEEM of protons or deuterons (green). Therefore, this contribution to the non-parametric rotation barrier distribution is irrelevant to the quantification of the ESEEM signal originating from methyl tunneling. The large confidence intervals of the corresponding tunneling ESEEM signal and the rotation barrier distribution in that region support our interpretation. From this analysis it becomes clear, that rotation barriers between 1500 K and  $\sim 2000$  K are responsible for the observed tunneling ESEEM (blue, purple in Fig. S2b–c), since their tunneling ESEEM signal matches the modulation depth and period of the fast decoherence contribution almost perfectly. Moreover, the confidence intervals of the tunneling ESEEM signal and the distribution are significantly smaller in the analyzed rotation barrier range.

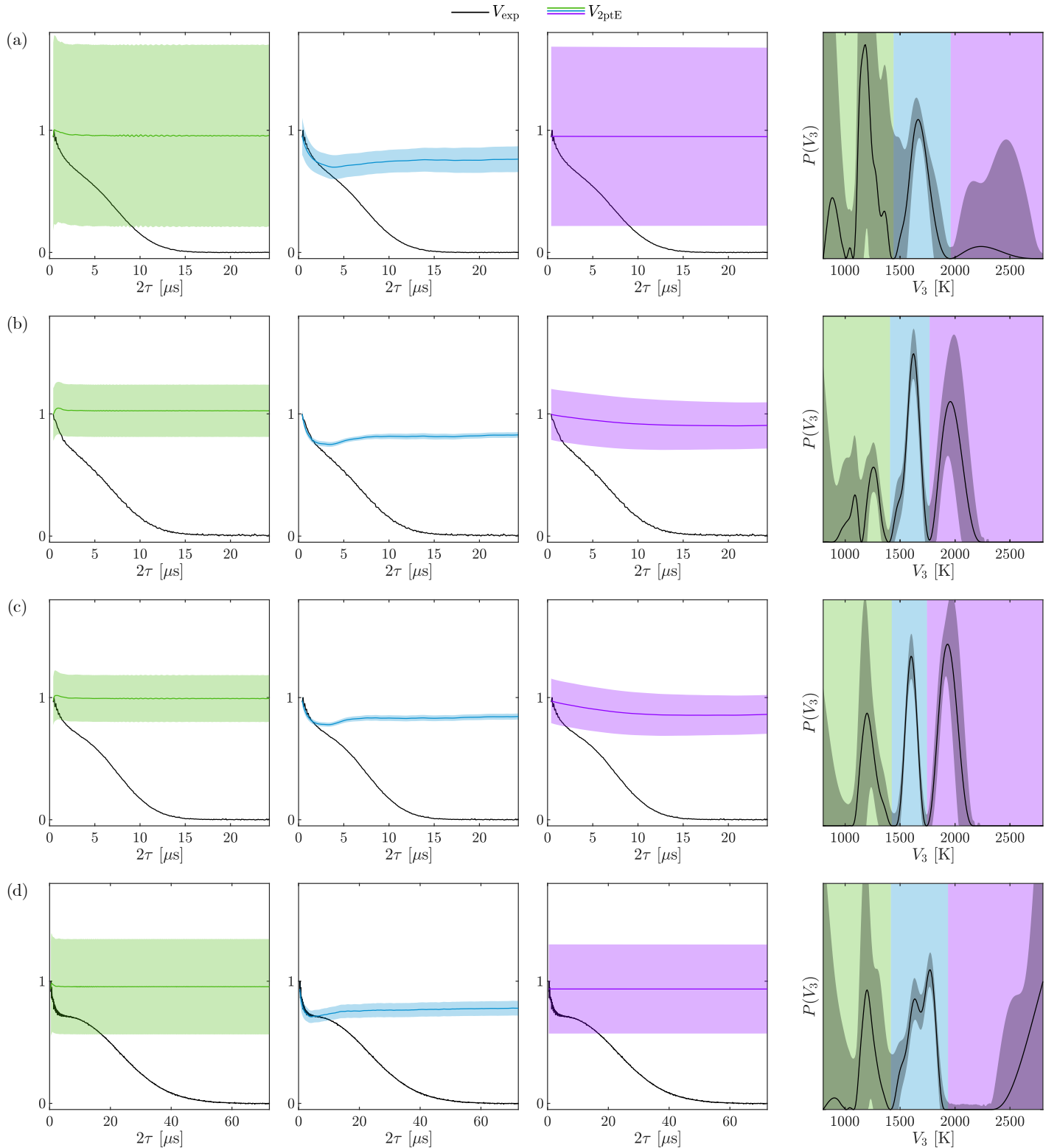


Fig. S2 Illustration of the ESEEM contributions present in the inferred non-parametric rotation barrier distribution. The experimental Hahn echo decay signal is illustrated in black as well as the extracted rotation barrier distribution. The green ESEEM contribution originates from rotation barriers in the range 800 K–1400 K. The blue ESEEM signal has its origin in the very certain region of the rotation barrier distribution between 1500 K and  $\sim$ 1800 K. The high rotation barrier range between  $\sim$ 1800 K and 2800 K is responsible for the purple ESEEM contributions. The experimental data, fitted distributions and ESEEM signals are given for 40 K (a) Q-band and (b) W-band measurements of H-mNOHex in OTP and for 10 K Q-band measurements of H-mNOHex in (c) OTP and (d) dOTP. We chose the regions individually for all data sets to separate prominent areas in each non-parametric rotation barrier distribution. The shaded areas of the ESEEM contributions as well as the gray areas of the rotation barrier distributions represent 95% covariance-based confidence intervals.

### S3 Influence of moving mean filter on deuterium nuclear ESEEM

We applied a moving mean filter using the `movmean`-function in DeerLab version 0.15.0dev<sup>2</sup> averaging the experimental data over 12 data points. Thereby, the nuclear ESEEM in the beginning of the Hahn echo decay signal is smoothed. After application of the filter, the first six points were cut, since the filter smooths all data points with equal sliding windows leading to unreasonable signal intensities at the beginning of the trace. The Gaussian rotation barrier distribution was inferred from the resulting Hahn echo decay signal without re-normalization of the data to ensure the modulation depth of the tunneling ESEEM is unchanged.

The time-domain fits for H-mNOHex in dOTP at 10 K at Q-band as well as the extracted Gaussian rotation barrier distributions from the unprocessed and the filtered experimental signal are illustrated in Fig. S3. It is visible in the fit residual, that the nuclear ESEEM at the beginning of the signal is not taken into account when fitting the rotation barrier distribution for the moving mean filtered trace. The fit quality is almost identical for both procedures. The Gaussian rotation barrier obtained from the filtered Hahn echo decay signal is narrower ( $\Delta\sigma \sim 70$  K) in comparison to the distribution extracted from the unprocessed data. The distribution inferred from the moving mean filtered data contains less probability density at low (below 1400 K) but also high rotation barriers (above 2000 K). In section S2, we attributed rotation barrier distribution mass below  $\sim 1400$  K to nuclear ESEEM modulations of the Hahn echo decay signal. In general, the moving mean filter helps to decrease the probability density in the low rotation barrier region between 1000 K and 1400 K which mask the nuclear deuterium ESEEM from the matrix deuterons.

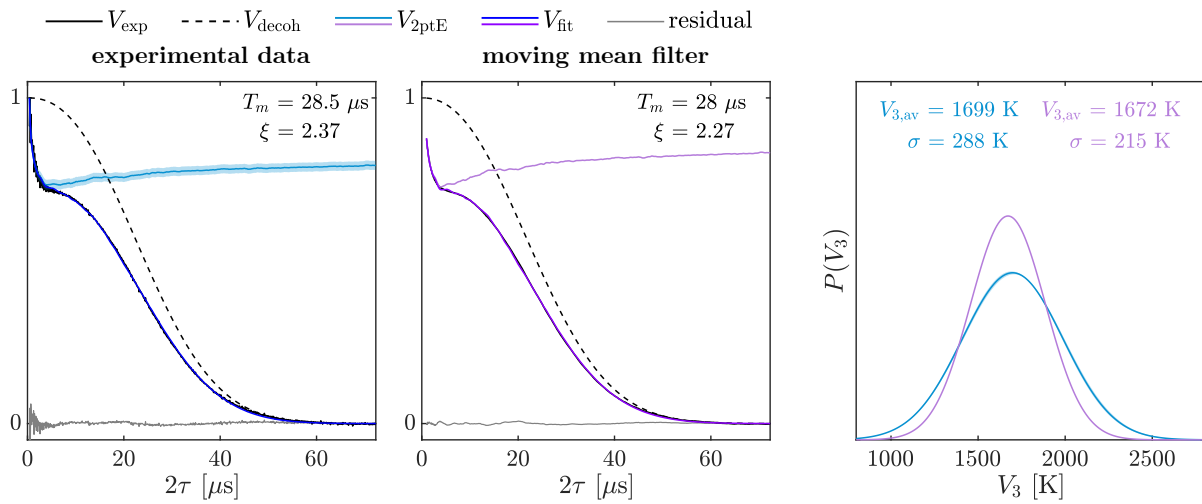


Fig. S3 Comparison of Gaussian rotation barrier distribution of H-mNOHex in dOTP extracted directly from the experimental data (left, blue) and after applying a moving mean filter to the recorded Hahn echo signal (middle, purple). The right panel represents the inferred Gaussian rotation barrier distributions and illustrates narrowing of the distribution upon application of the moving mean filter on the experimental signal. The shaded areas represent the bootstrapped 95%-confidence interval. The experimental data was recorded at 10 K at Q-band.

### S4 Temperature-dependent Hahn echo decay fits with a Gaussian distribution model

In this section we present all Hahn echo decay fits as well as the individually and globally extracted Gaussian rotation barrier distributions for H-mNOHex in OTP and dOTP for temperatures in the range of 10 K to 80 K evaluated using the MQR model. The Hahn echo decay fits and the individual rotation barrier distributions of H-mNOHex are shown for OTP in Fig.S4 and for dOTP in Fig.S5. The time-domain fits for both matrices and the globally inferred Gaussian rotation barrier distributions are presented in Fig. S6 and Fig. S7. A temperature-dependent comparison of the extracted Gaussian rotation barrier distributions is provided in Fig. S8.

### H-mNOHex in protonated matrix (OTP) - individual fits

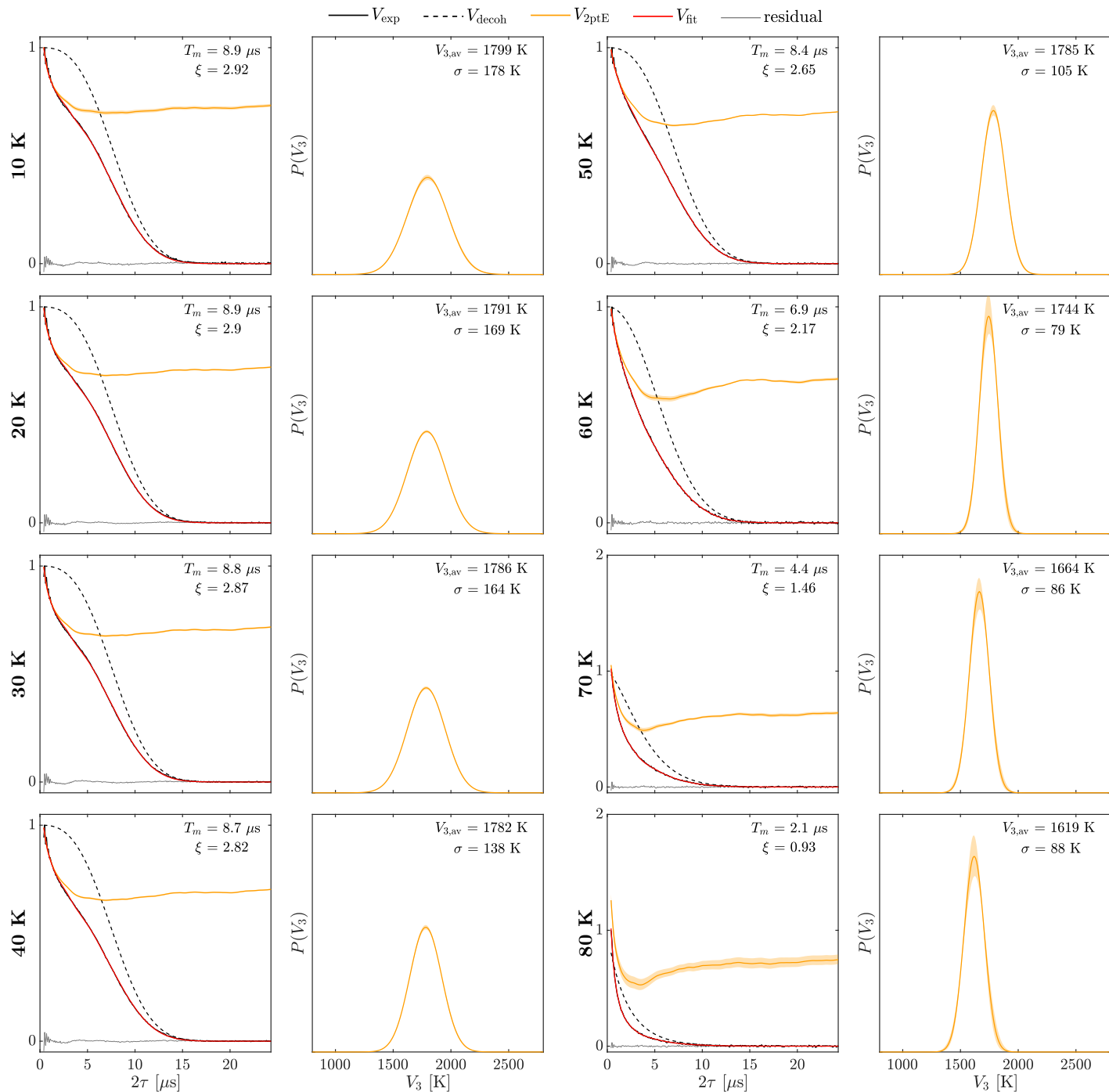


Fig. S4 Temperature dependence of the inferred Gaussian rotation barriers for H-mNOHex in OTP between 10 K and 80 K. For all temperatures, the left side always represents the experimental Hahn echo decay signal (black), the fitted matrix decoherence contribution (dashed), the fitted methyl tunneling contribution (orange) and the overall time-domain fit (red). The extracted Gaussian rotation barrier distribution is always illustrated on the right side. The shaded areas represent the bootstrapped 95%-confidence interval.

### H-mNOHex in deuterated matrix (dOTP) - individual fits

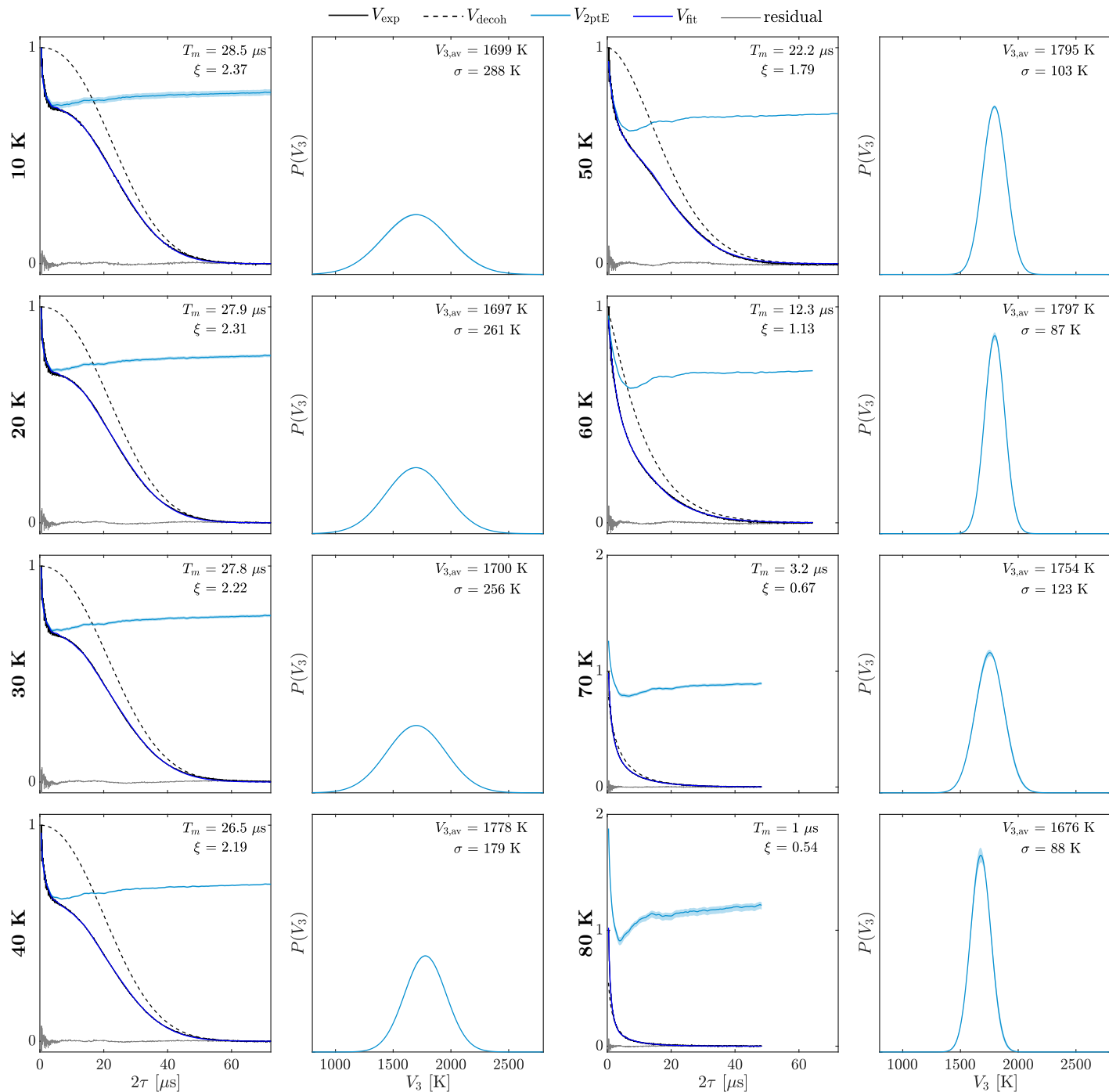


Fig. S5 Temperature dependence of the inferred Gaussian rotation barriers for H-mNOHex in dOTP between 10 K and 80 K. For all temperatures, the left side always represents the experimental Hahn echo decay signal (black), the fitted matrix decoherence contribution (dashed), the fitted methyl tunneling contribution (light blue) and the overall time-domain fit (blue). The extracted Gaussian rotation barrier distribution is always illustrated on the right side. The shaded areas represent the bootstrapped 95%-confidence interval.

### H-mNOHex in protonated (OTP) and deuterated matrix (dOTP) - global fits

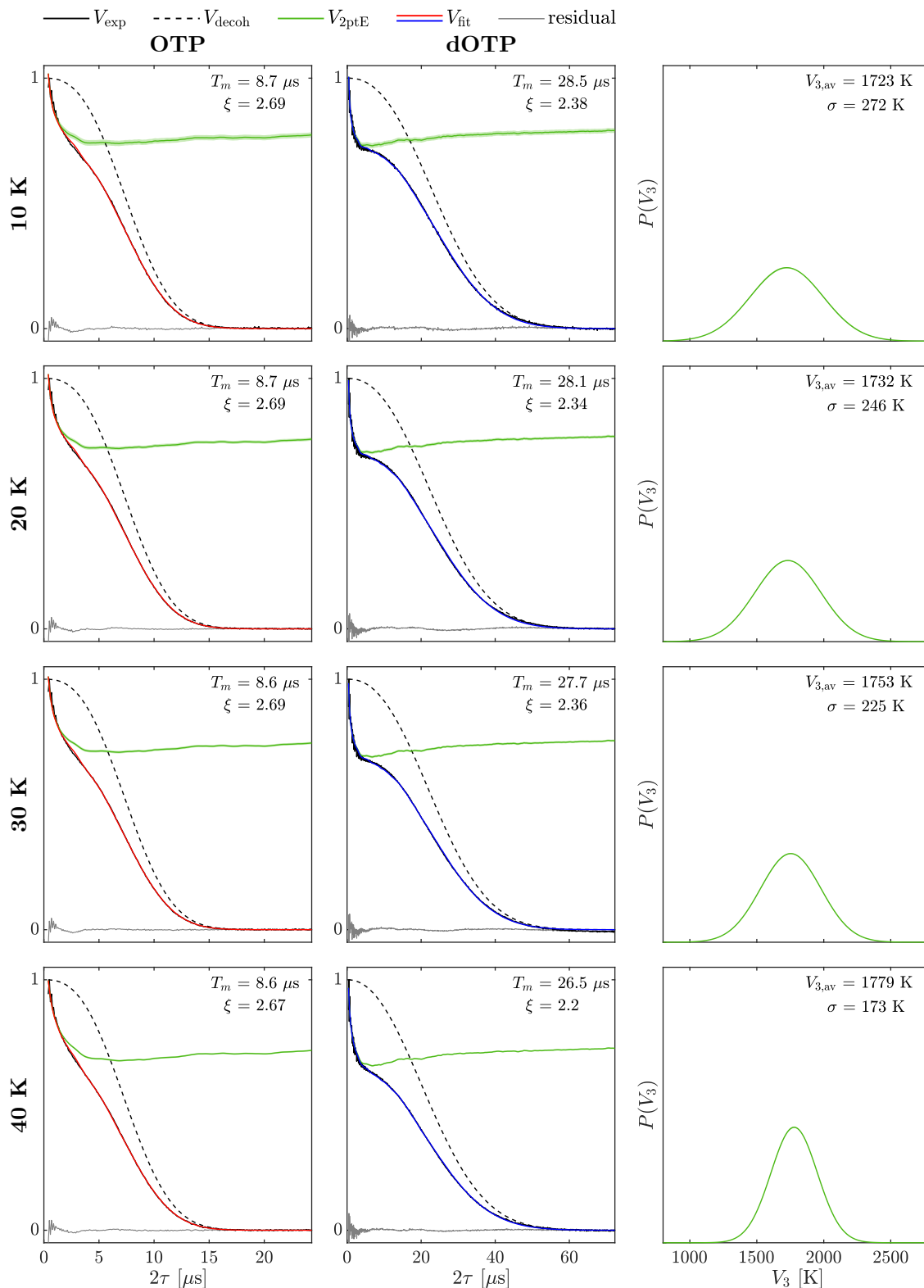


Fig. S6 Temperature dependence of globally inferred Gaussian rotation barriers for H-mNOHex in OTP and dOTP between 10K and 40K. For all temperatures, the left and middle panels represent the experimental Hahn echo decay signal (black), the fitted matrix decoherence contribution (dashed), the fitted methyl tunneling contribution (green) and overall time-domain fit (OTP, red - dOTP, blue). The extracted Gaussian rotation barrier distribution is always illustrated on the right side. The shaded areas represent the bootstrapped 95%-confidence interval.

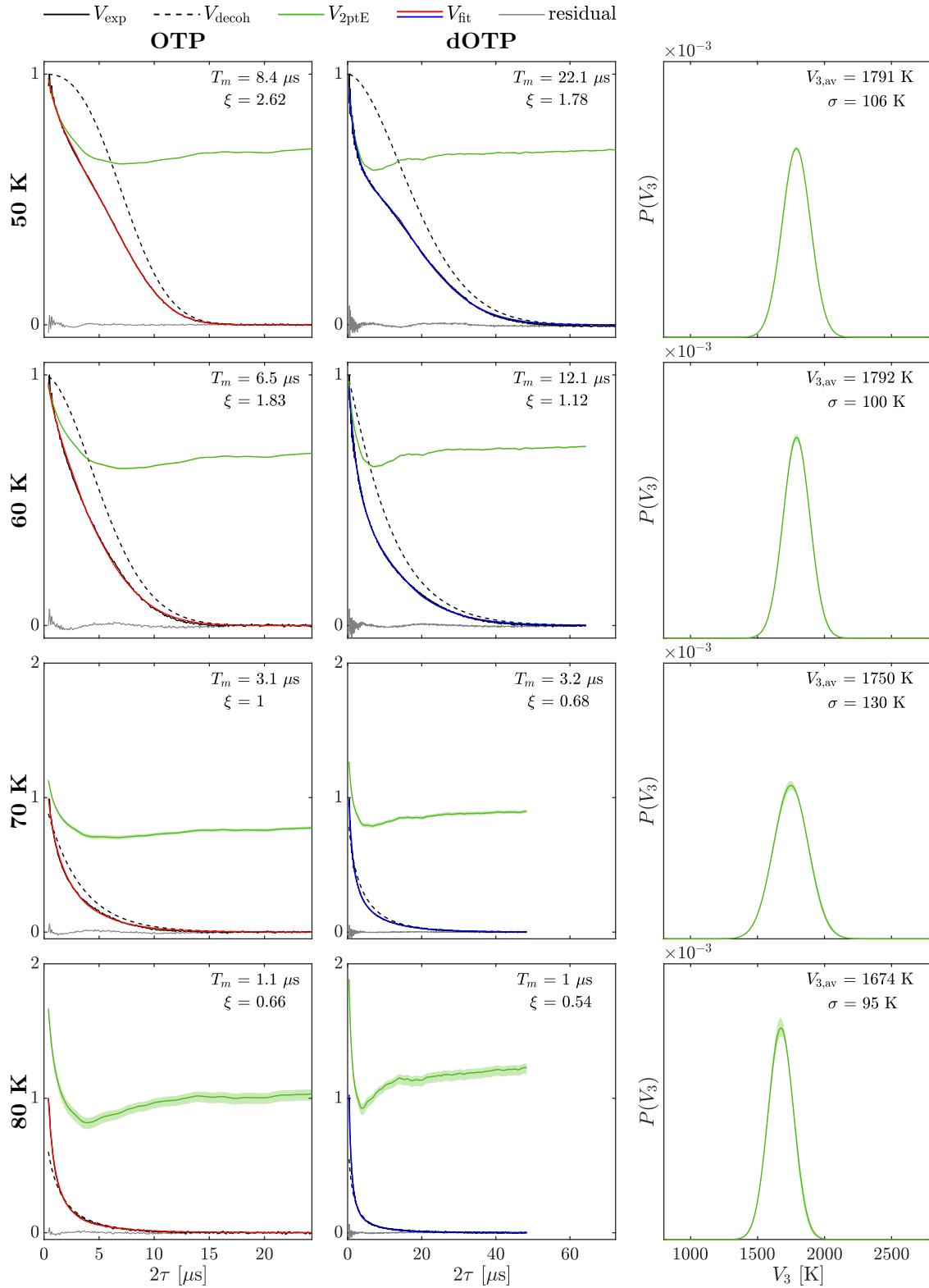


Fig. S7 Temperature dependence of globally inferred Gaussian rotation barriers for H-mNOHex in OTP and dOTP between 50K and 80K. For all temperatures, the left and middle panels represent the experimental Hahn echo decay signal (black), the fitted matrix decoherence contribution (dashed), the fitted methyl tunneling contribution (green) and overall time-domain fit (OTP, red - dOTP, blue). The extracted Gaussian rotation barrier distribution is always illustrated on the right side. The shaded areas represent the bootstrapped 95%-confidence interval.

## Comparison of individual and global rotation barrier distributions

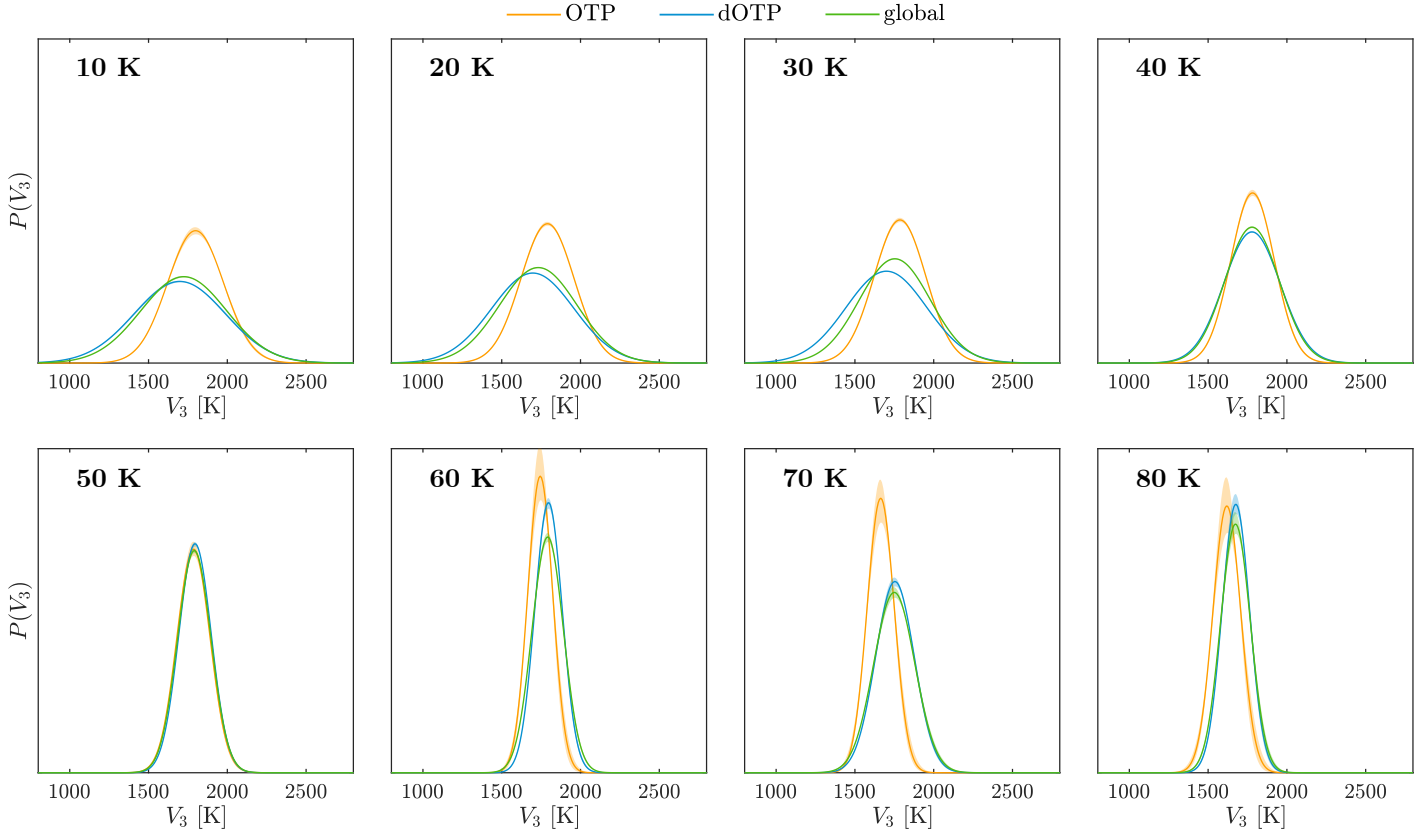


Fig. S8 Temperature dependence of the individually and globally inferred Gaussian rotation barrier distributions for H-mNOHex in OTP and dOTP measured between 10 K and 80 K. The distributions from the individual fits are given in orange for OTP and blue for dOTP as the matrix. The globally extracted rotation barrier distributions are shown in green. The shaded areas represent the bootstrapped 95%-confidence interval.

## S5 Influence of orientation averaging on tunneling ESEEM contribution

The Hamiltonian explaining the methyl tunneling ESEEM contribution to the Hahn echo decay signal is orientation dependent since it considers the hyperfine interaction between the methyl group protons and the electron spin (see chapter 2.1 in paper). Therefore, we

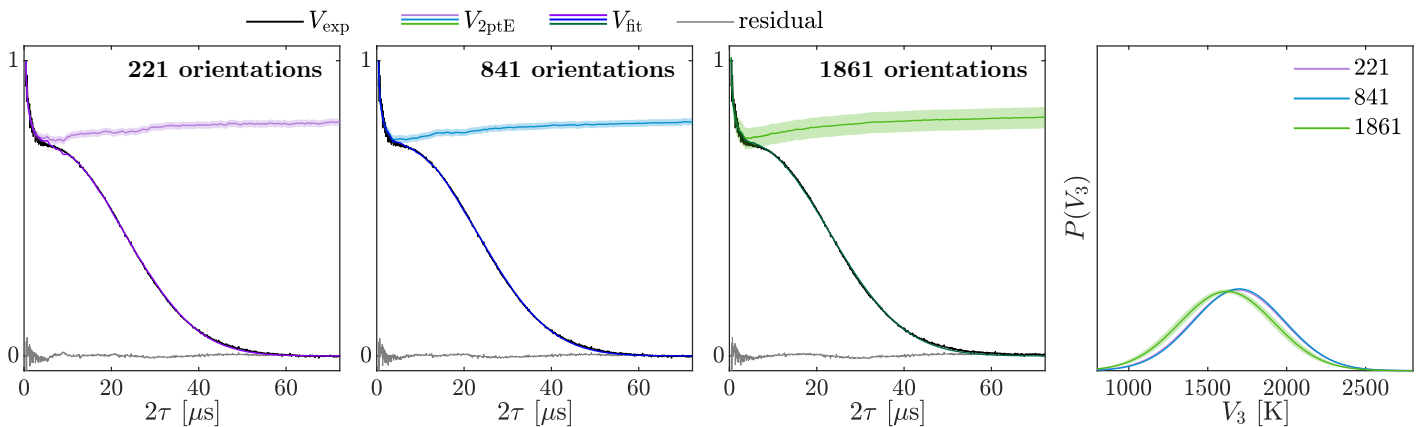


Fig. S9 Influence of varying sizes of the orientation grid considered for the tunneling ESEEM kernel. The experimental Hahn echo decay trace is fitted with kernels containing 221 (purple), 841 (blue) and 1861 (green) orientations of the nitroxide H-mNOHex in dOTP with respect to the external magnetic field. For insufficient orientation averaging with 221 orientations, an artificial bump is present in the tunneling ESEEM contribution between 5 and 10  $\mu\text{s}$  that vanishes when considering a larger grid of orientations. However, the inferred rotation barrier distribution shows only minor changes upon the different orientation grids. The shaded areas represent the bootstrapped 95%-confidence interval. The experimental data was recorded at 10 K at Q-band.

tested different sizes of the orientation grid by simulating tunneling ESEEM kernels containing 221, 841 and 1861 orientations of the nitroxide H-mNOHex in dOTP matrix with respect to the external magnetic field. We compare the fit quality of the MQR model and the inferred rotation barrier distribution for varying orientation grids in the kernel in Fig. S9. For 221 orientations, an artificial bump in the Hahn echo decay fit is introduced between  $2\tau = 5 - 10 \mu\text{s}$  from insufficient orientation averaging. The bump vanishes when taking into account more orientations. The orientation grid size has only a minor impact on the inferred rotation barrier distributions, which allows for fast and accurate inference of the rotation barrier distribution width for a small grid size. Still, for a deuterated matrix we advise to use at least 841 orientations in the kernel to avoid wrong interpretations of oscillations present in the fit residual.

## S6 Temperature-dependent comparison of SE, SSE and MQR model

In this section we compare the temperature dependence of the matrix relaxation contribution for H-mNOHex in either OTP and dOTP. We evaluated the phase memory time  $T_m$  by the stretched exponential (SE)<sup>3</sup>, sum of stretched exponential (SSE)<sup>3,4</sup> and methyl quantum rotor (MQR) model, respectively. The SE model considers a single stretched exponential described by

$$V_{\text{SE}}(2\tau) = \exp\left(-\left[\frac{2\tau}{T_m}\right]^\xi\right) \quad (17)$$

and in the SSE model the signal is modelled by two stretched exponentials according to

$$V_{\text{SSE}}(2\tau) = A \exp\left(-\left[\frac{2\tau}{T_{m,1}}\right]^{\xi_1}\right) + (1-A) \exp\left(-\left[\frac{2\tau}{T_{m,2}}\right]^{\xi_2}\right). \quad (18)$$

The parameter  $A$  in the SSE model can take values between 0 and 1 and weights the fast decaying contribution characterized by  $T_{m,1}$  and  $\xi_1$  and the matrix induced relaxation contribution parameterized by  $T_{m,2}$  and  $\xi_2$ . In the MQR model, the signal is modelled by the product of the methyl tunneling ESEEM signal and a stretched exponential function accounting for the matrix decoherence contribution.

The signal was normalized before fitting any of the models to the experimental data. When fitting the SE model, we isolate the matrix decoherence contribution by omitting the data points including the fast decoherence contribution. We present the results of the phase memory time ( $T_m$  and  $T_{m,2}$ ) in the temperature range from 10 K to 80 K fitted with the different models in Fig. S10. For interpretation of the results, we refer the reader to chapter 4.3 in the paper.

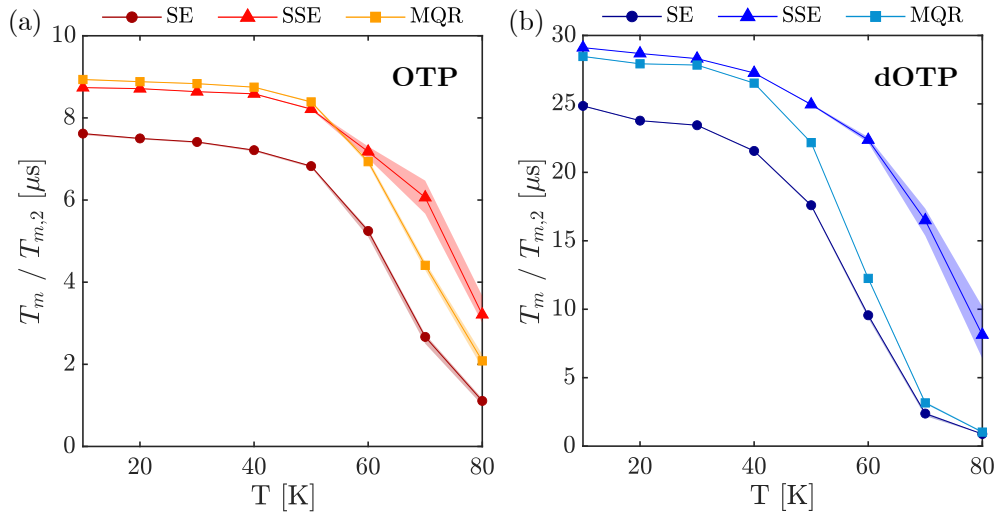


Fig. S10 Temperature dependence of phase memory time of the matrix decoherence contribution evaluated by different models for the Hahn echo decay of H-mNOHex in (a) OTP and (b) dOTP. Comparison of the phase memory time  $T_m$  describing the matrix relaxation contribution to the Hahn echo decay fitted by a stretched exponential (SE, circles), sum of stretched exponentials (SSE, triangles) and the here introduced methyl quantum rotor (MQR, squares) model.

## S7 Temperature dependence of low frequency oscillation in SE fit residual

Deuteration of the nitroxides geminal methyl groups decreases the tunneling frequency to the Hz-range, which is no longer detectable on the ESEEM timescale. Therefore, we compare Hahn echo decay traces of H-mNOHex with its deuterated equivalent D-mNOHex to identify the temperature range where methyl tunneling is the dominant proton position exchange process in a semi-quantitative manner. We used the SE model, which does not account for the fast relaxing contribution, to fit the experimental data of both spin systems in OTP. Afterwards, we performed a spectral analysis of the fit residual to identify frequencies that were not accounted by the SE model. Thus, the fit residual was apodized with a Hamming window prior to discrete Fourier transformation. The Hahn echo decay

fits, fit residuals and the resulting spectra are compared in Fig. S11 in the temperature range between 10 K and 80 K. We refer the reader to chapter 4.3 in the paper for a detailed interpretation of the semi-quantitative analysis.

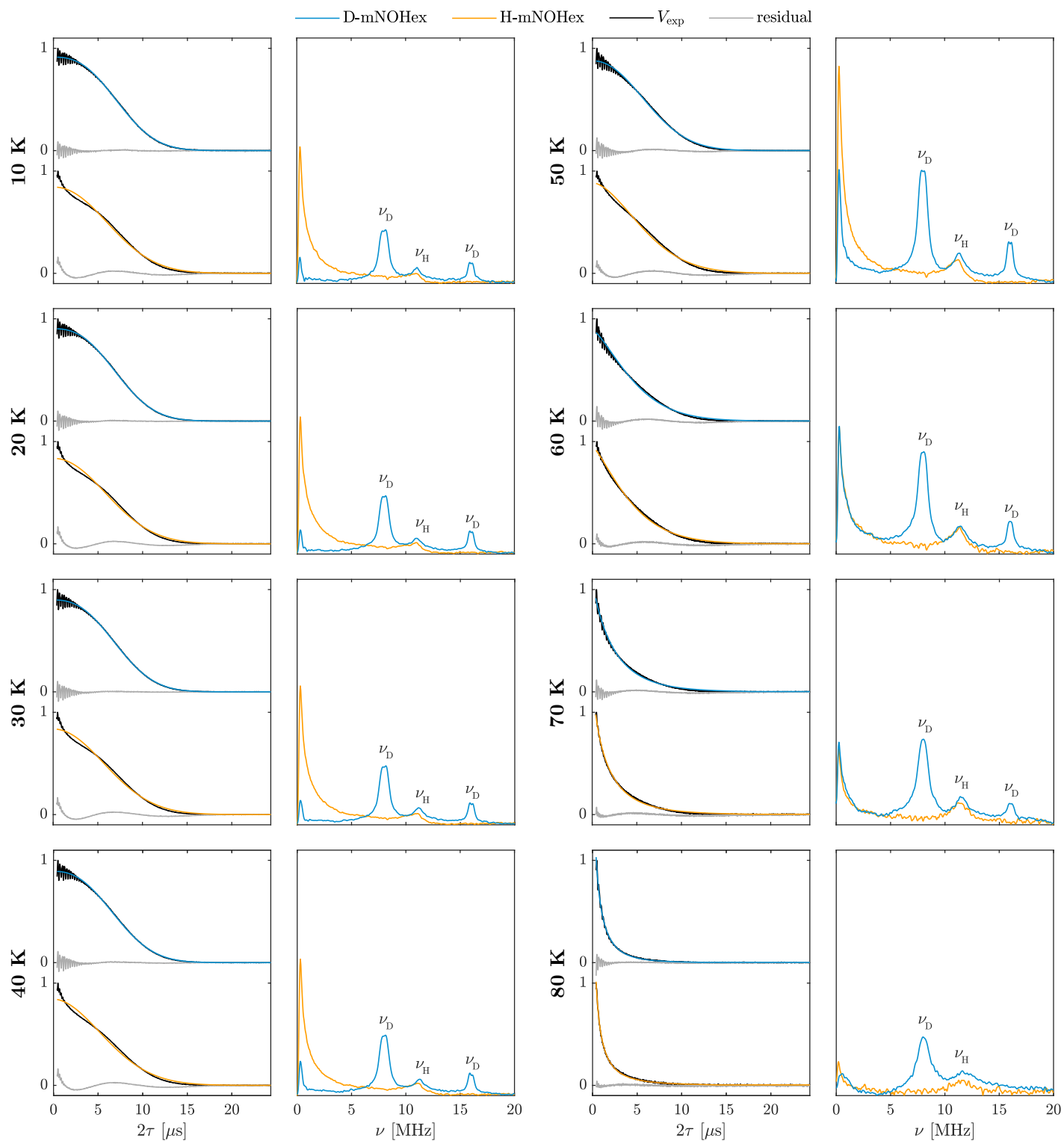


Fig. S11 Stretched exponential fit of Hahn echo decay traces and subsequent frequency analysis of the fit residual of H-mNOHex (orange) and D-mNOHex (blue) in OTP between 10 K and 80 K. For all temperatures, the left panel shows the experimental Hahn echo traces (black), the corresponding stretched exponential fits (orange, blue) and the resulting fit residual (gray). The right side illustrates the frequency spectrum of the Fourier transformed fit residuals. Common proton and deuterium nuclear ESEEM frequencies are marked by  $\nu_H$  and  $\nu_D$ , respectively.

## Notes and references

- 1 S. Khazaei and D. Sebastiani, *The Journal of Chemical Physics*, 2017, **147**, 194303.
- 2 L. Fábregas Ibáñez, G. Jeschke and S. Stoll, *Magnetic Resonance*, 2020, **1**, 209–224.
- 3 J. Soetbeer, M. Hülsmann, A. Godt, Y. Polyhach and G. Jeschke, *Physical Chemistry Chemical Physics*, 2018, **20**, 1615–1628.
- 4 J. Soetbeer, L. F. Ibáñez, Z. Berkson, Y. Polyhach and G. Jeschke, *Physical Chemistry Chemical Physics*, 2021, **23**, 21664–21676.